Origins of strain localization in a silver-based flexible ink under tensile load

Qiushi Li[1], Olivier Pierron[1,*] and Antonia Antoniou[1,*]

[1] The G.W. Woodruff School of Mechanical Engineering

Georgia Institute of Technology, Atlanta, GA, 30332-0405, USA

[*]Corresponding authors: olivier.pierron@me.gatech.edu and antonia.antoniou@me.gatech.edu

Abstract

Flexible electronics often employs composite inks consisting of conductive flakes embedded in a polymer matrix to transmit electrical signal. Recently, localized necking was identified as a cause of a substantial increase in normalized resistance with applied strain thereby adversely impacting electrical performance. The current study explores two possible contributing factors for the formation of such localization – ink surface roughness and local variations in silver flake volume fraction. Uniaxial tension experiments of a DuPont 5025 type ink are used to inform a constitutive model implemented using Finite Element Method (FEM) on different substrates. Surface roughness was modeled by sinusoidal variation in ink height, whose amplitude and wavelength are informed by experimental laser profilometry scan data. Local flake fraction variation obtained from experimental measurements before applying any strain, were modeled as local variations in the elastic modulus according to an inverse rule of mixtures between the silver flake and acrylic binder material properties. The study identified that the ink height roughness is the most impactful contributor to the subsequent strain localization. The substrate elastic properties impact the number and magnitude of localization bands, with the stiffer substrate delocalizing strain and averting catastrophic crack formation seen with a more compliant substrate. The model incorporating surface roughness closely matches experimental measurements of local strain across different substrates. The study can inform designers of the adverse impact of ink surface roughness on localization and subsequent detrimental increase of the resistance.

1. Introduction

Flexible electronic devices have gained considerable attention in recent years due to their increasingly widespread applications, including flexible displays (1-3), healthcare monitoring (4-

7), energy devices (8, 9), and implantable bioelectronics (10, 11). Compared with conventional silicon-based electronic devices, flexible electronics devices can be made wearable and have the advantages of flexibility, conformality, and ultralight weight (12, 13). However, an important challenge in the development of these devices is maintaining electrical performance when the device has been bent, twisted, or stretched to a high strain, typically up to 30% for a wearable device (14).

One strategy in devising a flexible electrical circuit involves printing a layer of conductive material, also called a conductive ink, onto a flexible polymer substrate. Different printing techniques, including screen printing (14-16), gravure patterning (17, 18), aerosol and ink-jet printing (19-23) have been used to deposit the conductive ink onto the polymer substrate. A common conductive ink design consists of filler conductive particles or flakes, typically of silver, being embedded in a polymer binder. The electrical performance of such conductive inks has been characterized in a number of studies (14, 19, 24, 25). However, unlike polymer supported thin metal films, whose mechanical behavior is fairly well understood from numerous experimental (26-37) and modeling (38-40) studies, there is currently limited knowledge specific to the mechanical behavior of these composite conductive inks (14, 24). An improved understanding of the inks' mechanical behavior will further the understanding of their electrical behavior under deformation and help inform their design. Cahn et al. (14) investigated the effect of strain localization on electrical conductivity in two types of composite conductive inks, both of which consisted of silver flakes embedded in a different binder material and screen printed onto a polymer substrates. Under uniaxial tensile strain, it was found that the normalized electrical resistance increased quickly with strain for the 5025 "flexible" ink with the acrylic binder, as seen in Fig. 1(a). Also, the electrical performance of the 5025 ink exhibited a substantial substrate sensitivity. Indeed, the electrical resistance increased much more rapidly with applied strain when the 5025 ink was deposited on a compliant substrate such as the thermoplastic polyurethane (TPU) TE11C than a stiff substrate such as polyethylene terephthalate (PET). Even if the ink had the same morphology before deformation, Fig. 1(b), there was evidence of a strong connection between electrical performance and deformation behavior. When the 5025 ink was deposited on the compliant TE11C substrate, it had a rapid normalized resistance increase, whilst exhibiting large through-thickness cracks at a low applied strain of 2.5%, Fig. 1(c)-(d). On the other hand, the 5025 ink deposited on the more stiff PET substrate, which showed superior electrical performance,

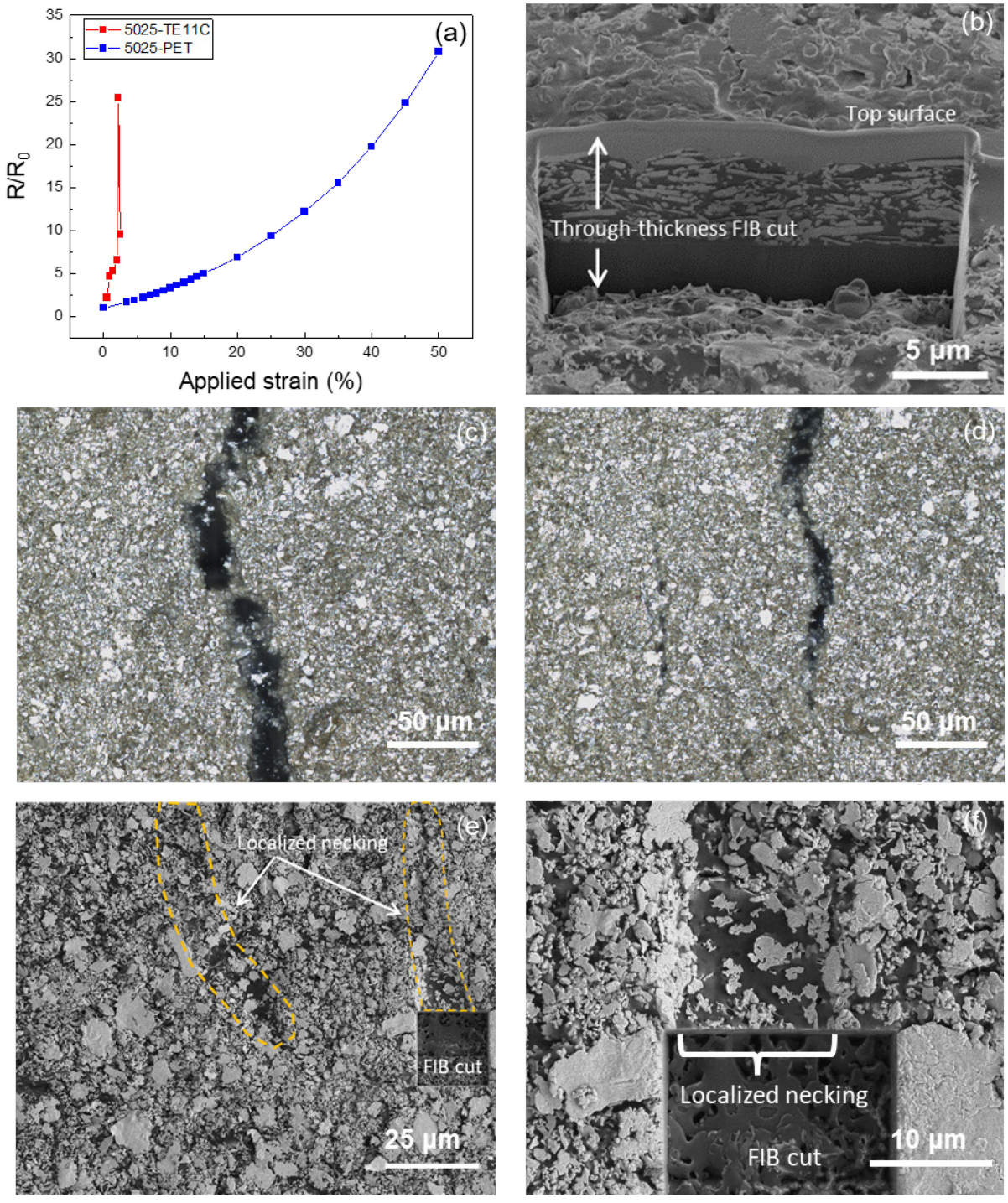

Figure 1. *(a) Normalized resistance as a function of applied strain for 5025 ink on PET and TE11C substrates; (b) SEM image of the undeformed 5025 ink showing the top ink surface roughness and through thickness ink morphology from a FIB cut.; (c)-(d) optical images of through-thickness cracks formed just after 2.5% applied strain for 5025 ink deposited on TE11C substrate; (e)-(f) SEM images highlighting localized necking areas formed after 35% applied strain for 5025 ink deposited on PET substrate. A FIB cut near a necked region showed a reduction in film height and silver flake fraction.*

developed localized necking without through-thickness cracking even at a high applied strain of 35%, as shown in Fig. 1(e)-(f). Therefore, the study revealed a substrate sensitivity wherein some combinations of ink/substrate would not be able to sustain applied strains beyond a few percent, whereas other combinations could go up to 30-40% applied strain without cracking. The study (14) also highlighted that the highly necked regions had undergone a change in the flake fraction as well as a thinning of the ink layer. It was suggested by Cahn et al. (14) that the localized necking exhibited by the 5025 ink was more detrimental to electrical conductivity than surface cracks that are observed in other ink types. Since localized necking is so detrimental to electrical performance, it is important to identify the key contributing factors to their formation in composite hybrid inks. The current study explores the origin of such localized necking in the 5025 ink. Specifically, the study explores whether the ink's spatially varying flake fraction or the fluctuating ink height (surface roughness) are contributing to the localized necking. The study achieves this with an experimentally informed finite element (FE) model exploring the origins of localized necking in the 5025 ink and substrate sensitivity.

2. Experimental and modeling procedures

2.1. Experimental procedure

A 5025 conductive ink formulated by DuPont is composed of silver flakes embedded in an acrylic binder material. The average volume fraction of silver flakes in the ink is about 49% (14). The 5025 ink test specimens consist of a layer of the 5025 ink screen printed onto a polymer substrate layer in a single printing pass. The ink is printed in double trace lines with a 2 mm trace width (Fig. 2(a)). The screen printing process was performed at the Dupont Applications Laboratory with processes that have been optimized for the ink and substrates considered. The 5025 ink layer is about 9 μm thick, which is much thinner than the polymer substrate layer with a nominal thickness of 127 μm for the PET substrate and 89 μm for the TE11C substrate. The polyethylene terephthalate (PET) is chosen as the substrate material for the experiments due to its high stiffness, which appeared to forestall the cracking and loss of electrical conductivity that had been observed to occur with more compliant substrates at low applied strains (14). Several different experiments with 5025 ink-on-PET specimens are presented in the current work. These experiments inform the

construction of finite element (FE) models investigating the origins of strain localization as well as provide a point of comparison for the FE modeling results.

2.1.1. Uniaxial tension experiment

Uniaxial tension experiments were performed on a number of 5025 ink-on-PET specimens as well as on bare PET specimens to obtain the 5025 ink's stress-strain response. The experiments were performed on the Linkam Scientific TST350 Microtensile Test Stage at a crosshead speed of 30 μm/s. The ink's stress-strain response is calculated using a simple subtraction of tensile force data measured from the ink-substrate and bare substrate specimens, Fig. 2(c). Due to PET's high

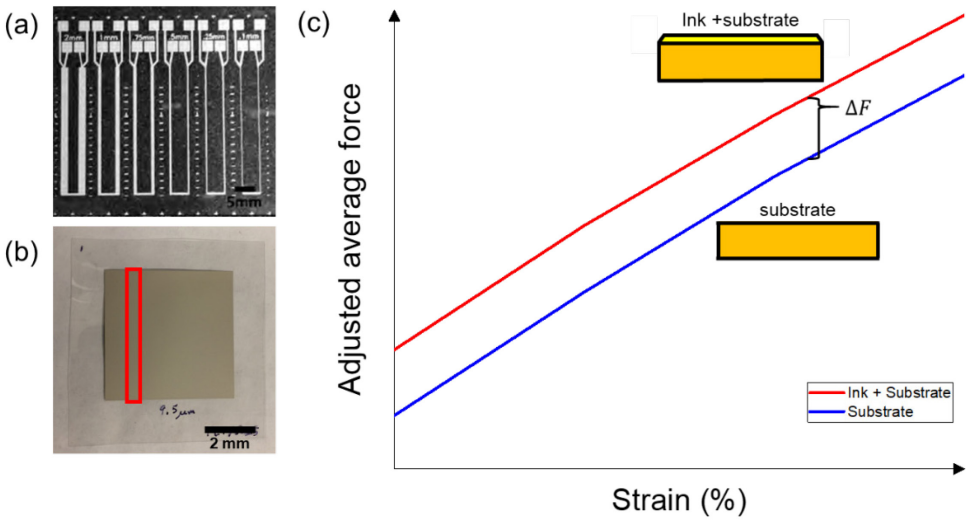

Figure 2. *(a) Optical image of 5025 on TE11C substrate with different labeled trace widths; (b) Optical image of unpatterned 5025 ink on PET substrate with approximate specimen dimensions for tension test labeled in red. (c) Schematic drawing showing the force subtraction method for calculating the ink stress-strain response.*

stiffness, a large amount of noise is encountered with the data collected using the conventional specimens with trace lines. To make more accurate calculations, unpatterned 5025 ink-on-PET specimens, as seen in Fig. 2(b), were used instead of the conventional specimens with trace lines. After normalizing the tensile force data for each specimen with respect to the narrowest specimen width, an average adjusted force is calculated for both the 5025-PET and bare PET specimens. The ink's stress-strain response is then calculated by subtracting the average adjusted force for the bare PET specimens from that for the 5025-PET specimens, as shown in the Fig. 2(c) schematic.

2.1.2. *In-situ* uniaxial tension experiment

Results of the *in-situ* uniaxial tension experiment with a 5025 ink-on-PET specimen performed by Cahn et al. (14) were further examined in this work. Cahn et al. performed the *in-situ* uniaxial tension experiment on a 5025-PET specimen with 2 mm trace width using the Linkam Scientific TST350 Microtensile Test Stage at a crosshead speed of 50 μm/s. Optical images with approximate dimensions 200 × 200 μm and spatial resolution 0.25 μm/pixel were taken at various applied strain increments using an Olympus LEXT 4100 confocal microscope. The images were processed using the open source digital image correlation (DIC) software Ncorr (41) to generate the in-plane strain maps along the stretch direction.

2.1.3. Laser profilometry scan of surface roughness

Laser profilometry scans were performed using an Olympus LEXT 4100 confocal microscope to characterize the surface topography of the 5025 ink screen printed on PET substrate. The scanned area was 256 × 256 μm and the spatial resolution was 0.25 μm/pixel.

2.2. Modeling procedure

To study the origins of strain localization, two-dimensional finite element (FE) models were constructed for the freestanding ink and ink-substrate systems under uniaxial tension (Fig. 3). The

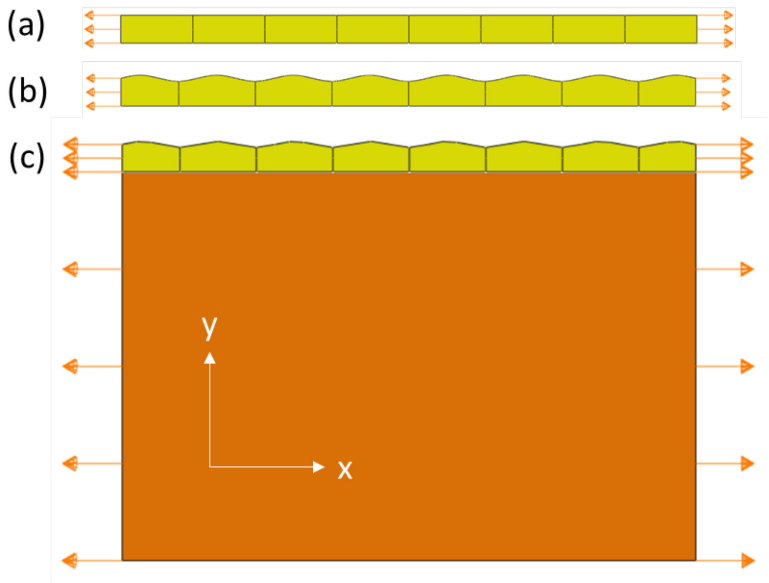

Figure 3. *Schematic drawings of different FE models and boundary conditions for (a) freestanding ink with uniform height; (b) freestanding ink with height variations; (c) ink-substrate system with ink height variations.*

boundary conditions consist of the modeled system having the x direction displacement applied uniformly on both the left and right edges in uniaxial tension. The ink-substrate interface is held by a tie constraint and has frictionless, hard contact conditions. Plane strain conditions are assumed for the ink-substrate models, and quadrilateral plane strain elements are used. The mesh of the ink layer is partitioned into a number of regions to accommodate for the assignment of different material properties for the modeling of silver flake fraction variations. A mesh sensitivity study was performed to identify that the approximate element size used is 0.5 μm in the ink layer and 1 μm in the substrate layer, as seen in Supplementary Material.

The FE models were used to test the hypothesis, put forward in the current study, that there are two possible causes of strain localization: surface roughness and local variations in silver flake volume fraction. In the absence of these two factors, the ink's stress-strain response is assumed to be elastic-perfectly plastic, resembling the ink's stress-strain response on a PET substrate. The models will be exploring the cause for the initial creation of localization (less than <10% applied strain).

In the absence of both surface roughness and variation in the flake fraction, the ink layer model has a uniform height (thickness) of 9 μm, seen in Fig. 3(a), and a uniform flake fraction of 49% throughout the ink layer according to experimental observations described by Cahn et al. (14). Surface roughness is modeled as sinusoidal height (thickness) variations along the ink layer's top edge, Fig. 3(b). The default amplitude (1 μm) and wavelength (25 μm) of the ink height variations are approximate averages based on the laser profilometry scan data of a 5025-PET specimen. The PET substrate layer has a uniform height (thickness) of 127 μm and the TE11C substrate has a uniform height thickness of 89 μm, both of which are based on average measured thicknesses. The default overall length of the model with surface roughness wavelength of 25 μm is 187.5 μm, comprising of 7.5 wavelengths. A summary of the geometric dimensions and material properties used in the models is given in Table 1.

Local silver flake volume fraction variations are modeled by partitioning the ink layer into a series of regions along its length, seen in Fig. 3, for which different flake fractions are assigned according to the normal distribution with an average of 49% and standard deviation of 9% (14). This normal distribution was experimentally measured from the initial flake fraction in the through thickness direction, seen in Fig. 1(b). The local elastic modulus for the composite ink is assumed to vary with local silver flake fraction according to the inverse rule of mixtures.

$$E_{comp} = \left(\frac{\varphi_{Ag}}{E_{Ag}} + \frac{1 - \varphi_{Ag}}{E_{acrylic}} \right)^{-1} \quad (1)$$

Here E_{comp} is the modulus of the composite, φ_{Ag} is the silver flake volume fraction, E_{Ag} is the elastic modulus for silver, and $E_{acrylic}$ is the elastic modulus for the acrylic binder material. The composite ink elastic modulus E_{comp} was assumed to be 1.66 GPa at the average 49% flake fraction as calculated from the uniaxial tension experiments, and 76 GPa at 100% flake fraction or pure silver (42). The acrylic binder material elastic modulus $E_{acrylic}$ is back calculated from E_{comp} at 49% flake fraction and E_{Ag} to be 0.86 GPa, which is close to the lower bound of elastic modulus for commercially available acrylic materials. The yield strength was assumed to be 22.6 MPa, as calculated from the uniaxial tension experiment, throughout the ink layer regardless of the local flake fraction. The yield strengths of both pure silver and pure acrylic are generally cited to be above 50 MPa (43, 44), which is significantly higher than the measured ink yield strength of 22.6 MPa. In the absence of a method to accurately relate the local ink yield strength to the local flake fraction, it is assumed that the ink yield strength is 22.6 MPa throughout the ink layer regardless of the local flake fraction.

Table 1. Geometric dimensions and material properties for FE models

	Average model height (y dimension, μm)	Model length (x dimension, μm)	Roughness amplitude (um)	Roughness wavelength (um)	Number of periods	Material	Elastic modulus	Poisson's ratio	Yield strength
Ink (yellow)	9	187.5 (default); depends on number of periods used for model	1 (default); varies between 0.5 and 2	25 (default); varies between 6 and 50	7.5 (default)	5025 ink	1658 MPa (5025 ink)	0.37 (5025 ink)	22.6 MPa (5025 ink)
Substrate (orange)	127 (PET), 89 (TE11C)					TE11C, PET	75.1 MPa (TE11C), 3022 MPa (PET)	0.48 (TE11C), 0.40 (PET)	0.931 MPa (TE11C), 54.0 MPa (PET)

3. Results

3.1. Experimental results

The experimental results needed to inform the FEM modeling are presented in this section. Specifically, the following sections describe the extracted 5025 ink uniaxial stress strain response, the ink strain fields during uniaxial stretch, and the roughness of the ink surface *before* uniaxial experiments are performed.

3.1.1 Uniaxial tension experiments

Figure 4 shows the 5025 ink's stress-strain response calculated by subtracting the average adjusted force of the bare PET specimens from that of the 5025 ink screen printed on PET. The ink stress-strain data and standard deviation are based on measurements from 3 different experiments for each condition. The raw data from such experiments can be found in the Supplementary Material section. The 5025 ink's stress-strain response essentially resembles an elastic-perfectly plastic behavior. The elastic modulus E = 1.66 GPa was obtained by linear regression fitting of the data points up to 1.4% strain, which is taken to be the yield strain. Beyond 1.4% strain, the stress no

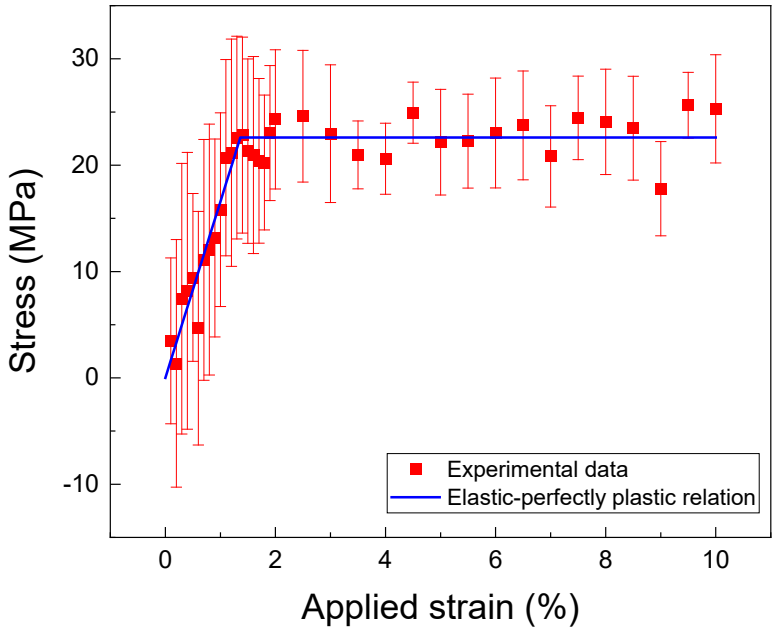

Figure 4. *Experimentally measured uniaxial stress-strain response for 5025 ink. The ink response was obtained using the force subtraction method comparing the response of PET with and without 5025 ink. The standard deviation is from at least three experiments.*

longer appears to increase linearly with strain and the ink response is approximately that of a perfect plastic material. A yield strength of 22.6 MPa was obtained by averaging the values over the plateau. The elastic modulus and yield strength obtained from the uniaxial tension experiments were used as input material properties for the FE modeling of the 5025 ink. The ink constitutive behavior is implemented in the FE models as seen in Fig. 4.

3.1.2 Strain maps from *in-situ* uniaxial tension experiment

Optical images were taken during the *in-situ* uniaxial tension experiment with the 5025 screen printed on PET substrate. These were analyzed to obtain in-plane strain maps along the loading direction for various applied strain increments. Figure 5 shows such in-plane tensile strain maps as well as local strain data normalized with respect to the applied strain plotted along the marked paths (i), (ii), (iii) for the applied strains 5%, 10%, and 15%. At 5% applied strain, the normalized

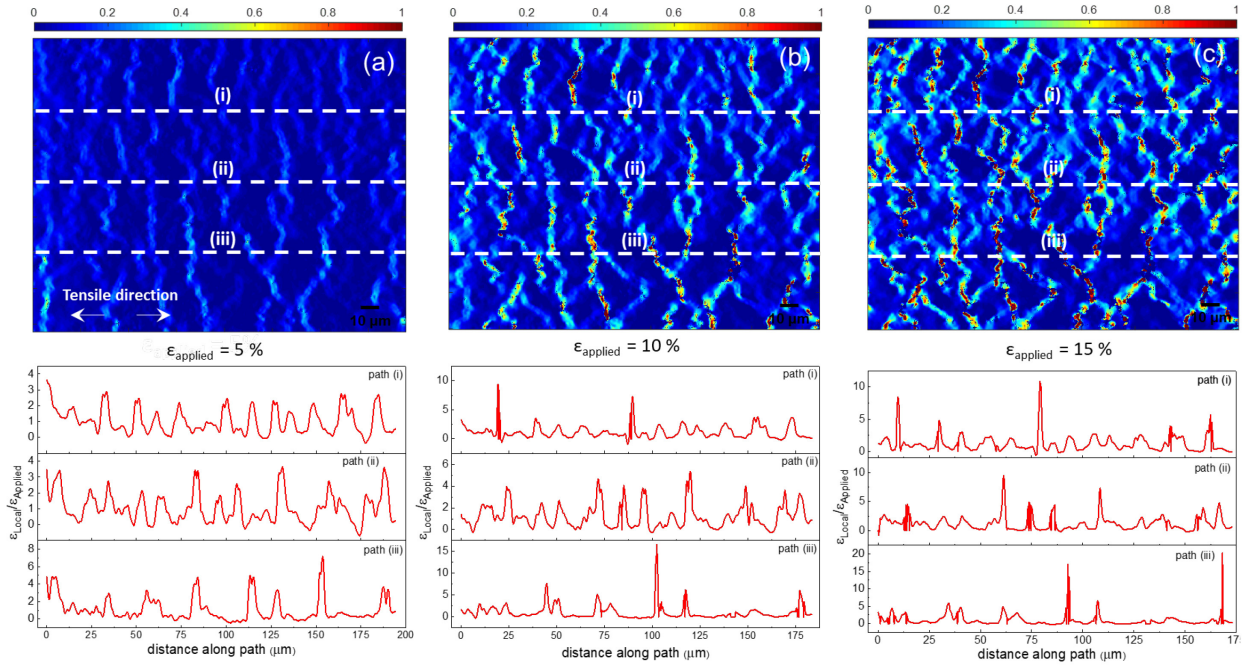

Figure 5. *Experimental in-plane strain maps for 5025 ink deposited on PET substrate along the tensile direction at (a) 5%, (b) 10%, (c) 15% applied strains. Below each map, line plots of the local strain normalized by the applied strain along marked paths (i)-(iii).*

local strain plots show a series of strain localization peaks about 15 μm apart with magnitudes about 3 times the applied strain. At 10% applied strain, the normalized local strain plots show a

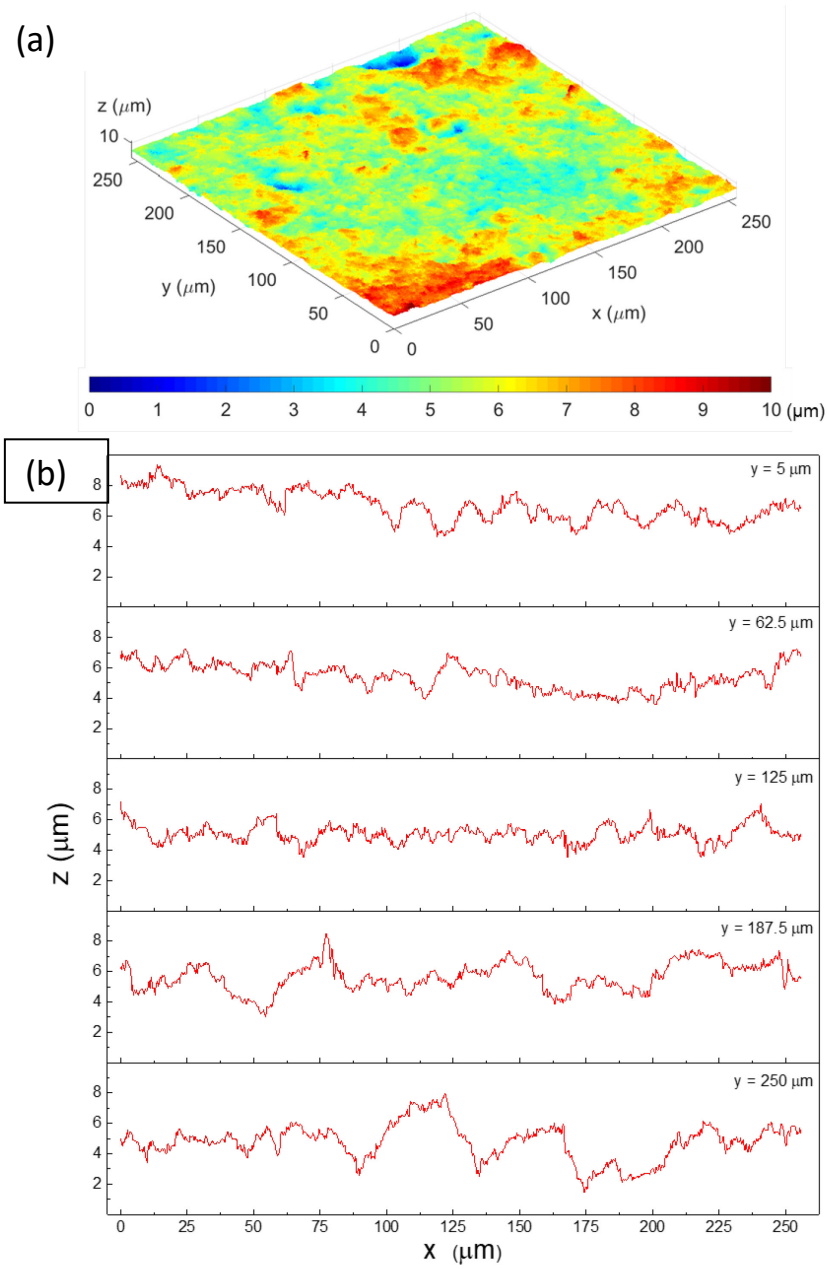

Figure 6. *(a) Colored map of height data from profilometry scan of the surface of 5025 ink screen printed on a PET substrate; (b) Line plots of height data along x direction at various y increments*.

greater variation in the magnitude of the strain localization peaks. There is a bifurcation into high peaks with normalized local strains of above 10 and low peaks with normalized local strains near zero is observed along path (i) and (iii). At 15% applied strain, the normalized local strain plots along all three paths show further concentration of strain localization into fewer locations with much higher normalized local strains. The onset of instability in strain localization occurs beyond an applied strain of 10%, at which a transition appears to be occurring from the relatively numerous, dispersed areas of strain localization to the relatively fewer, highly localized necks.

3.1.3. Laser profilometry scan of initial surface roughness

Figure 6 shows the results of the laser profilometry scan for the undeformed surface of the 5025 ink screen printed on PET substrate. The x and y directions are marked on the scan colored map. Figure 6(a) shows a colored surface topography map over a 256 × 256 μm area of the 5025 ink surface. Figure 6(b) shows the ink height data along the x direction at various y position increments. If the surface roughness is modeled with sinusoidal waves, the amplitude a appears to range from 0.5 to 3 μm and the wavelength λ appears to range from 6 to 50 μm. At y position increments of 187.5 μm and 250 μm, the wavelength and amplitude of the surface roughness appear to be significantly larger than those measured at the other y position increments, indicating significant local variations in the magnitude of surface roughness in different regions of the ink surface. Similar variations in surface roughness were observed in laser profilometry measurements with other 5025 ink specimens, and here we made the informed assumption that the surface roughness measured in Figure 6 was generally representative of such variations.

3.2. Finite element (FE) modeling results

The FE models focus on the investigation of the two hypothesized origins of strain localization for the 5025 ink screen printed on polymer substrates under uniaxial tension – surface roughness and variations in local silver flake volume fraction. The impact of roughness and flake fraction on different substrate materials as well as the effects of varying surface roughness parameters are also examined. The results are mostly presented as two-dimensional tensile strain distribution maps and plots of local tensile strain data normalized with respect to the applied strain against the projected x direction along the top surface of the ink layer so as to provide a direct comparison

with the experimental in-plane strain maps from the *in-situ* uniaxial tension experiment.

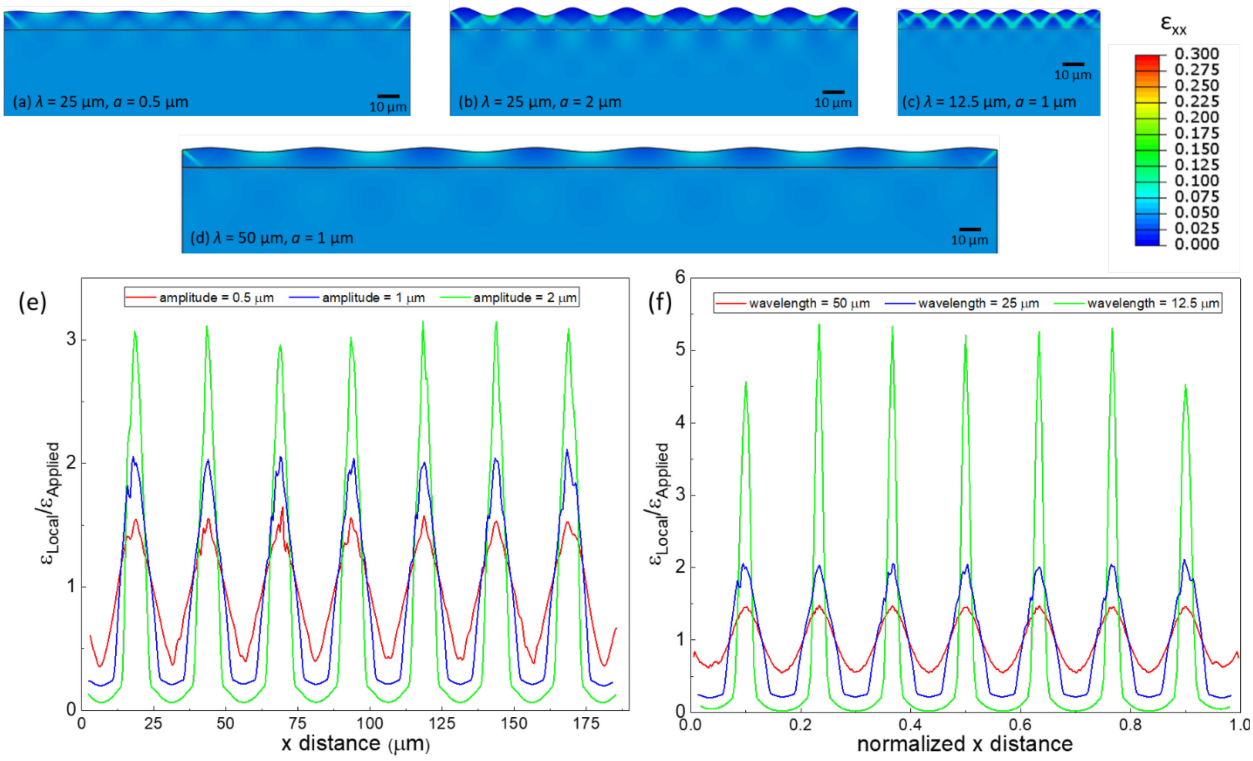

Figure 7. *FE model tensile strain maps for 5025-PET at 5% applied strain for roughness amplitude (a) 0.5 μm and (b) 2 μm at constant wavelength of 25 μm, for roughness wavelength (c) 12.5 μm and (d) 50 μm at constant amplitude of 1 μm; normalized local strain along ink layer top surface vs projected x at 5% applied strain for various (e) roughness amplitudes at constant wavelength of 25 μm and (f) roughness wavelengths at constant amplitude of 1 μm. The scale bar is the same for all strain map sets shown (a)-(d).*

3.2.1 Effect of ink surface roughness wavelength and amplitude

The effect of surface roughness amplitude *a* and wavelength λ on possible strain localization in the 5025-PET at 5% applied strain is shown in Fig. 7. The different amplitudes and wavelengths used were informed from the profilometry scan data shown in Fig. 6. The study of the varying amplitudes from 0.5 to 3 μm were performed with a constant wavelength of 25 μm. The study of varying wavelength from 12.5 to 25 μm was performed with a constant amplitude of 1 μm. We note that unless otherwise specified, the default simulation conditions correspond to λ = 25 μm and a = 1 μm.

At 5% applied strain, the normalized local strains are greater for larger amplitudes and shorter wavelengths. If one were to describe the sinusoidal surface roughness as stress concentrators in the form of a series of notches, the severity of the notch can be described by the stress concentration factor k_t as defined by the ratio between the maximum local stress at the notch root to the nominal stress without the stress concentrator. For a series of sinusoidal notches located along the edge of an infinite half-plane, Savruk et al. (45) found k_t to be a function of the ratio between the sinusoidal amplitude and wavelength.

$$k_t \approx 1 + [1 + 1.5\tanh(0.3\ln\gamma + 0.7)]\sqrt{\gamma} \quad (2)$$

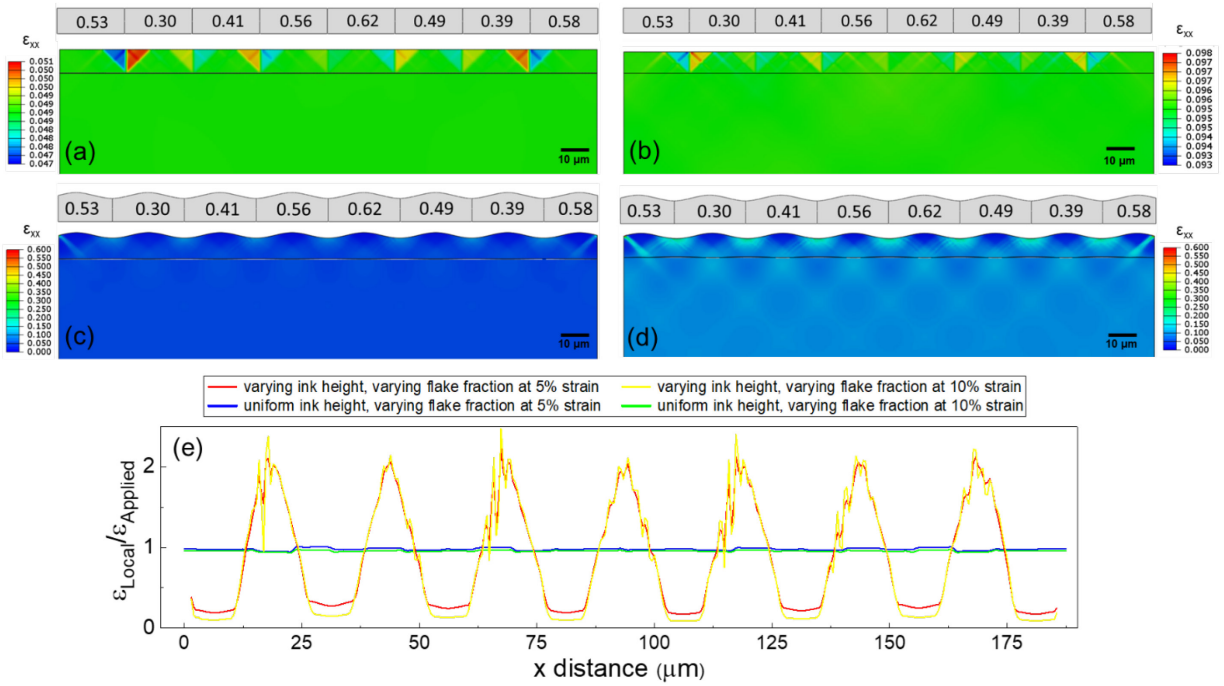

Figure 8. *FE model tensile strain maps for 5025-PET at (a) 5% and (b) 10% applied strains, with uniform ink height but varying flake fraction. Tensile strain maps at (c) 5% and (d) 10% applied strains, for FE models with both varying ink height (with wavelength 25 μm and amplitude 1 μm) and varying flake fraction. The flake fraction variation is imposed by partitioning the film into different regions shown at the top of each sub-image. (e) The normalized local strain along the ink layer top surface versus projected x distance for the two different combinations of surface roughness and flake fraction at 5% and 10% applied strains.*

Here the ratio γ is equal to 4 times the a/λ ratio. Therefore, the stress concentration factor from doubling the amplitude, a is the same as that from halving the wavelength, λ. While the above analytical model can provide guidance, it is not expected to describe the behavior of finite films.

3.2.2 Effect of silver flake volume fraction variation

Figure 8 examines the impact of local flake fraction variation on local strains with and without surface roughness for 5025-PET at 5% and 10% applied strains. Flake fraction variation is implemented by assigning to the different mesh partitions of the ink layer model different elastic moduli. If the ink height is kept uniform and only the flake fraction (i.e. modulus) is allowed to vary then, as seen in Fig. 8(a)-(b), there is no local strain variation from the applied strain, at both 5% and 10% applied strains. Therefore, the initial local flake fraction is not the dominant cause of the localized necking. When both ink height variation and the flake fraction variation are present, Fig. 8(c)-(d) shows that the ink height variation is much more dominant in initiating sites of local elevated strain from the applied. The flake fraction (modulus) on the other hand caused only minor fluctuations in local strain.

3.2.3 Effect of ink surface roughness with different substrates

Figure 9 shows how the local strain that develops on the rough ink surface with and without the presence of a substrate layer. The sinusoidal surface roughness for all the models has a wavelength λ of 25 μm and amplitude a of 1 μm. The FE model tensile strain maps are arranged with decreasing substrate moduli from left to right (5025-PET on the left, 5025-TE11C in the center, and freestanding 5025 ink on the right) and increasing applied strains from top to bottom. The applied strains shown for the three substrate cases are different due to the differing magnitude of local strain in the ink layer for the different substrate cases. The bottom row shows the normalized local strain along the top surface of the ink layer plotted against the project x distance. The freestanding ink (Fig. 9(i-l)) exhibited the highest localized strain, about 40 times the applied strain of 2% at a single location, corresponding to the cracking and fracture of the ink layer. When the 5025 ink is screen printed on a substrate, more of the ink height minima experienced elevated local strains, but these elevated local strains were never as high as that for the freestanding ink. For the more compliant TE11C substrate, the elevated local strain is uniform at each height minima for 1% applied strain, but for 3% and especially 6% applied strain the local strain for one of the height minima became significantly higher than the others. Compared with the freestanding 5025 ink, the

magnitude of the local strain for 5025 on TE11C is lower and the concentration of strain localization toward a single location occurs at a higher applied strain. For the stiffest substrate case—the PET, the elevated local strains at multiple height minima on the ink surface remain uniform up to 10% applied strain. The magnitude of the localization remains relatively low compared to the other substrate cases.

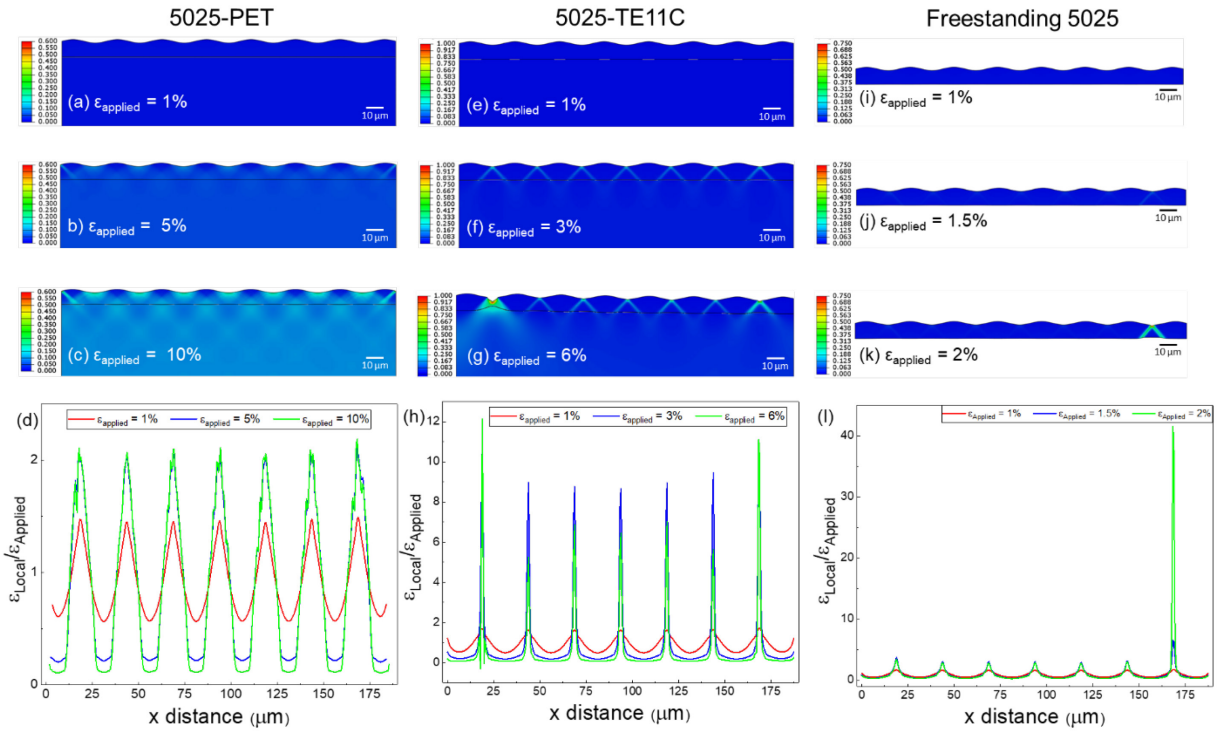

Figure 9. *Tensile strain maps of FE models with ink height variations (wavelength 25 µm and amplitude 1 µm) for (a)-(c) 5025-PET, (e)-(g) 5025-TE11C and (i)-(k) freestanding 5025 ink at different applied strains. Bottom row shows the normalized local strain versus the projected x distance at various applied strains for (d) 5025-PET, (h) 5025-TE11C and (l) freestanding 5025 ink.*

The presence of a stiffer substrate contributes to decreasing the local strain at the height minima of the ink surface. This allows the specimen to stretch to a higher applied strain without cracking or fracture. As seen in Fig. 7, the local strain amplitude is also impacted by the wavelength and amplitude of the roughness. Qualitatively, it appears that halving λ resulted in a higher normalized local strain than doubling a despite both cases having the same stress concentration factor according to Eq. (1). This discrepancy could be explained by the fact that the ink layer is not an

infinite half-plane but is a relatively thin layer mounted on a substrate. Therefore, Eq. (1) needs to be adjusted to incorporate film and substrate thickness and elastic property mismatch before it can be applied to predict the enhancement in strain. The current study shows that due to a stiff substrate like PET having a strong delocalizing effect on deformation in the ink layer, having a lesser substrate effect such as in the case of halving λ and keeping a constant leads to comparatively higher strain localization.

4. Discussion

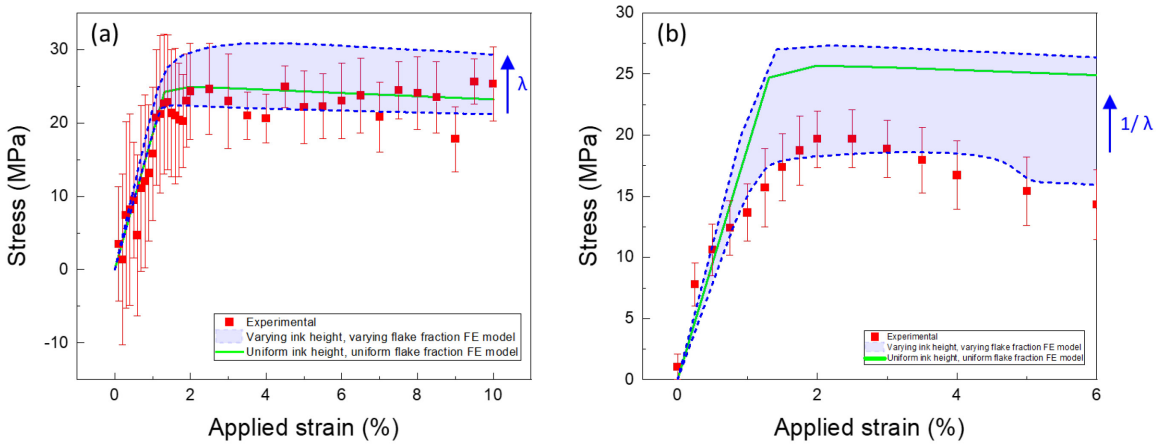

Figure 10 *Comparison of the experimental and numerical (FE) stresses on 5025 ink screen printed on (a) PET and (b) TE11C substrates. For the FE models, the stress-strain response was extracted from nodal reactive forces for the various FE models with uniform or varying ink height and flake fraction.*

4.1. Stress-strain relationship of the 5025 ink

We have demonstrated that severe strain localization observed at low applied strains in the 5025-TE11C specimen was mainly induced by surface roughness with a minor influence from the modulus variation from the flake fraction. When the deformation is sufficiently delocalized as in the case of the 5025-PET specimen, it was assumed that the stress-strain response of the ink layer should approach that in the practical absence of strain localization. This assumption was tested for the 5025-PET and 5025-TE11C FE models by comparing the stress-strain responses (extracted from nodal reactive forces in the ink layer) in the presence and in the absence of the two aforementioned strain localization factors. In Figure 10, these results from the FE models are shown together with the experimental 5205 ink stress-strain responses calculated using force

subtraction for both the 5025-PET and 5025-TE11C cases. The FE ink response in the absence of the two strain localization factors, shown as the green line, is basically an elastic-perfectly plastic one with the entire ink layer thinning uniformly both before and after yielding. The range of FE ink stress-strain responses in the presence of the two strain localization factors is shown as the region bounded by the blue dashed lines. The range is obtained from models with different ink height amplitudes and wavelengths according to those observed in Fig. 7, since surface roughness is a far more dominant factor than flake fractions according to the current model. It is worth pointing out that for the same a/λ ratio the FE ink stress response was generally higher for 5025-PET models with larger wavelengths λ but lower for 5025-TE11C models with larger λ. This could be understood by the role of the substrate in delocalizing deformation and modulating the stress field in the ink layer. When λ is large and the a/λ ratio is small, the strain localization is more strongly impacted by the substrate due to the relatively greater length of the thin sections of the ink layer near the ink height minima. A stiff substrate such as the PET delocalizes deformation to a large extent, resulting in less strain localization and a higher stress response with increasing λ. A compliant substrate such as TE11C has a poor ability to delocalize deformation, resulting in greater strain localization and a lower stress response with increasing λ.

As shown in Figure 10(a), the FE ink stress-strain response extracted from the 5025-PET model in the absence of strain localization, shown as the green line, is generally close to that in the presence of strain localization, whose range forms a relatively narrow envelop around it. Also, for the 5025-PET models the FE ink responses in the presence of strain localization do not show noticeable softening. Like Figure 10(a), Figure 10(b) used an elastic-perfectly plastic constitutive relation as input data for the 5025 ink with an elastic modulus of 1.66 GPa and yield strength of 22.6 MPa, but the FE ink stress-strain responses were extracted from the 5025-TE11C model rather than the 5025-PET model. In the absence of strain localization, the FE ink stress-strain responses with uniform ink height and uniform flake fraction were the same for the 5025-PET and 5025-TE11C models. However, in the presence of strain localization the FE ink responses from the 5025-TE11C model had a much wider range as well as a significant apparent softening behavior toward the lower bound of the range. This behavior matches the experimental stress-strain data obtained from 5025-TE11C specimens quite well, though the ink material property input data were based on the 5025-PET experiments and the apparent softening was caused by surface roughness-induced strain localization. Given the lack of apparent softening behavior and relative closeness

to the FE ink response in the absence of strain localization, the FE ink responses from the 5025-PET models in the presence of strain localization appear to validate the approach of using experimental 5025 ink stress-strain data measured from the 5025-PET specimens to calibrate the ink's constitutive relation in the absence of strain localization for the FE models.

4.2. Factors inducing and influencing strain localization

According to the current FE model, the ink surface roughness—a geometrical effect, appears to affect strain localization the most. The material properties of the ink itself, such as the variations in silver flake fraction, appear to play a secondary role. The magnitude of the strain localization is modulated by the thickness and material properties of the substrate, most notably the elastic modulus. For the two substrate materials considered in the current work, PET has an elastic modulus of ~3 GPa, which is about twice that of the 5025 ink, while TE11C has an elastic modulus of 75.1 MPa, which is about 5% that of the 5025 ink (Table 1). SEM images in Figure 1(c)-(d) showed that the 5025 ink screen printed on TE11C substrate developed cracking at a low applied strain of 2.5%, while the FE modeling results in Figure 7(e)-(h) showed that an instability in the strain localization had clearly developed by 6% applied strain. By contrast, for the 5025 ink screen printed on PET both *in-situ* experimental (Fig. 5) and FE modeling results (Fig. 7(a)-(d)) at 5% applied strain showed a series of relatively uniform strain localizations have developed with local strains that are about 2-3 times the applied strain. At 10% applied strain (Fig. 5(c)), however, the *in-situ* experimental results showed the onset of instability in the ink's strain localization, which was not present in the corresponding FE modeling results.

Prior analytical studies on metallic films deposited on different substrates (39, 46-49) have shown that under sinusoidal surface perturbations, the critical strain ε_C for the loss of ellipticity and localization (in this case formation of shear bands) for a material following power-law strain hardening with strain hardening exponent N is:

$$(\varepsilon_C - N)^2 - \frac{4N\varepsilon_C}{\exp(4\varepsilon_C)-1} = 0 \tag{3}$$

For a material with a small N, the critical strain ε_C is approximately $\sqrt{N}$. An elastic-perfectly plastic material has a N of 0, and the onset of instability is expected at an applied strain equal to the yield strain.

When the 5025 ink is mounted on a stiff substrate such as the PET, the onset of instability is modulated by the substrate material rather than the ink. The strain hardening exponent for the PET material used in the experiments can be estimated to be about 0.1, with the critical strain for the onset of instability being roughly 30%. While the 5025-PET FE model with surface roughness predicts no onset of instability at 10% applied strain, the experimental strain maps appeared to show an onset of instability at this level of applied strain. The cause(s) for the early onset of instability in the 5025 ink on PET still await further investigation. Possible causes may include larger than expected local variations in surface roughness or very drastic local variations in silver flake volume fraction. *Ex-situ* experiments performed at 35% strain also showed flake-matrix debonding (14), so it is also possible that the debonding initiates at ~10% applied strain. Future *in-situ* experiments under a scanning electron microscope (SEM) could help reveal more details of the ink's deformation behavior at a higher resolution.

When both surface roughness and flake fraction variation are present in the FE model, surface roughness had been shown to be the far more dominant factor in affecting both global and local strains for the range of applied strains considered (up to 10%). In the uniform ink height model, local flake fraction variations alone could still cause some minor strain localization much smaller in comparison to those caused by surface roughness. However, it should be noted that in the current model only the elastic modulus was made to vary with the local flake fraction. If the yield strength is also found to vary significantly with the local flake fraction, the level of strain localization could potentially be higher, although surface roughness likely would still be the main factor in determining strain localization (Supplemental Material 3).

5. Summary and Conclusions

The current work investigated two possible causes of strain localization (necking) in 5025 ink–surface roughness modeled as sinusoidal ink height variations and local variations in silver flake volume fraction modeled as local variations in elastic modulus, using finite element method modeling informed by experimentally determined material properties. The following conclusions can be drawn from the current results.

1. The stress-strain response of the 5025 ink on the PET substrate could be obtained by a subtraction of the averaged measured force of the bare PET specimens from that of the

5025-PET specimens under the uniaxial tension. The ink is shown to exhibit an elastic nearly perfect plastic response with a modulus of ~1.7 GPa, a yield stress of 22.6 MPa.

2. The ink surface roughness, implemented in the FE models as a sinusoidal perturbation with amplitude and wavelength based on experimental surface topography measurements, was shown to have a substantial effect on the formation of localized necking. Without height variation, the inks exhibited uniform thinning with applied strain and no localization. Local flake fraction variations, modeled as impacting the ink elastic modulus according to an inverse rule of mixtures between silver and acrylic, had a secondary effect.
3. Both in-plane strain maps obtained from the *in-situ* uniaxial tension experiments of 5025 on PET tested under the confocal microscope as well as the surface strain from FE models incorporating surface roughness showed strain localization at multiple sites. This occurred for 5025 ink on PET and such sites had uniform normalized localized strain of about a factor of 2 to 3 times the applied strain at low applied strains (≤ 5%). At an applied strain of 10% and 15%, the *in-situ* in-plane strain maps showed instability and a transition towards more localized necking.
4. The stiffness of the substrate material played an important role in delocalizing deformation in the 5025 ink. Both experimental and FE modeling results showed that a substrate material with stiffness comparable to or greater than that of the 5025 ink, such as PET, had a much greater ability to delocalize deformation in the ink than a substrate that is much more compliant than the 5025 ink, such as the TE11C.

The above study can be useful to explain the origin of substrate-induced variations in the resistance measurements for 5025 ink and to propose possible mitigation methods to minimize the detrimental effect of necking. For example, methods to control ink height variations during screen printing process before the curing step occurs can substantially reduce the resistance increase with applied strain, without compromising the ability of the ink to remain intact at high applied strains.

Acknowledgements

The authors gratefully acknowledge funding support from the National Science Foundation (NSF CMMI-MOMS: 2026936). The authors are grateful to DuPont colleagues (Jeff Meth, Lynne Dellis and Augustus Jones) for providing samples.

Conflicts of Interest

The authors declare no conflicts of interest.

References

1. Kim et al. S. Low-power flexible organic light-emitting diode display device. Advanced Materials. Advanced Materials. 2011;23(31):3511-6.
2. Rogers et al. JA. Paper-like electronic displays: Large-area rubber-stamped plastic sheets of electronics and microencapsulated electrophoretic inks. Proceedings of the National Academy of Sciences. 2001;98(9):4835-40.
3. Sekitani et al. T. Stretchable active-matrix organic light-emitting diode display using printable elastic conductors. Nature materials. 2009;8(6):494-9.
4. Gao et al. W. Fully integrated wearable sensor arrays for multiplexed in situ perspiration analysis. Nature. 2016;529(7587):509-14.
5. Imani et al. S. A wearable chemical–electrophysiological hybrid biosensing system for real-time health and fitness monitoring. Nature communications. 2016;7(1):1-7.
6. Lee et al. H. A graphene-based electrochemical device with thermoresponsive microneedles for diabetes monitoring and therapy. Nature nanotechnology. 2016;11(6):566-72.
7. Schwartz et al. G. Flexible polymer transistors with high pressure sensitivity for application in electronic skin and health monitoring. Nature communications. 2013;4(1):1-8.
8. Dubal et al. DP. Towards flexible solid-state supercapacitors for smart and wearable electronics. Chemical Society Reviews. 2018;47(6):2065-129.
9. Lv et al. T. Nanocarbon-based materials for flexible all-solid-state supercapacitors. Advanced Materials. Advanced Materials. 2018;30(17).
10. Hong et al. YJ. Wearable and implantable devices for cardiovascular healthcare: from monitoring to therapy based on flexible and stretchable electronics. Advanced Functional Materials. 2019;29(19).
11. KIm et al. D. Materials for multifunctional balloon catheters with capabilities in cardiac electrophysiological mapping and ablation therapy. Nature materials. 2011;10(4):316-23.
12. Gu et al. Y. Mini review on flexible and wearable electronics for monitoring human health information. Nanoscale research letters. 2019;14(1):1-15.
13. Cai et al. S. Review on flexible photonics/electronics integrated devices and fabrication strategy. Science China Information Sciences. 2018;61(6):1-27.
14. Cahn G, Barrios A, Graham S, Meth J, Antoniou A, Pierron O. The role of strain localization on the electrical behavior of flexible and stretchable screen printed silver inks on polymer substrates. Materialia. 2020;10.
15. Merilampi S, Laine-Ma T, Ruuskanen P. The characterization of electrically conductive silver ink patterns on flexible substrates. Microelectronics reliability. 2009;49(7):782-90.
16. Shin D-Y, Lee Y, Kim CH. Performance characterization of screen printed radio frequency identification antennas with silver nanopaste. Thin Solid Films. 2009;517(21):6112-8.
17. Sung D, de la Fuente Vornbrock A, Subramanian V. Scaling and optimization of gravure-printed silver nanoparticle lines for printed electronics. IEEE Transactions on Components and Packaging Technologies. 2009;33(1):105-14.
18. Kim S, Sung HJ. Effect of printing parameters on gravure patterning with conductive silver ink. Journal of Micromechanics and Microengineering. 2015;25(4).
19. Borghetti M, Serpelloni M, Sardini E, Pandini S. Mechanical behavior of strain sensors based on PEDOT: PSS and silver nanoparticles inks deposited on polymer substrate by inkjet printing. Sensors and Actuators A: Physical. 2016;243:71-80.
20. Van Osch TH, Perelaer J, De Laat AW, Schubert US. Inkjet printing of narrow conductive tracks on untreated polymeric substrates. Advanced Materials. 2008;20(2):343-5.

21. Yang W, Mathies F, Unger EL, Hermerschmidt F, List-Kratochvil EJ. One-pot synthesis of a stable and cost-effective silver particle-free ink for inkjet-printed flexible electronics. Journal of Materials Chemistry C. 2020;8(46):16443-51.
22. Schlisske S, Raths S, Ruiz-Preciado LA, Lemmer U, Exner K, Hernandez-Sosa G. Surface energy patterning for ink-independent process optimization of inkjet-printed electronics. Flexible and Printed Electronics. 2021;6(1):015002.
23. Tafoya RR, Secor EB. Understanding effects of printhead geometry in aerosol jet printing. Flexible and Printed Electronics. 2020;5(3):035004.
24. Merilampi S, Björninen T, Haukka V, Ruuskanen P, Ukkonen L, Sydänheimo L. Analysis of electrically conductive silver ink on stretchable substrates under tensile load. Microelectronics Reliability. 2010;50(12):2001-11.
25. Krawczyk KK, Groten J, Glushko O, Krivec M, Frühwirth M, Schulz G, et al. Self-Reducing Silver Ink on Polyurethane Elastomers for the Manufacture of Thin and Highly Stretchable Electrical Circuits. Chemistry of Materials. 2021;33(8):2742-55.
26. Bautista JR, Avilés F, Oliva AI, Ceh O, Corona JE. Correlations between mechanical stress, electrical conductivity and nanostructure in Al films on a polymer substrate. Materials characterization. 2010;61(3):325-9.
27. Hommel M, Kraft O. Deformation behavior of thin copper films on deformable substrates. Acta Materialia. 2001;49(19):3935-47.
28. Lacour SP, Wagner S, Huang Z, Suo Z. Stretchable gold conductors on elastomeric substrates. Applied physics letters. 2003;82(15):2404-6.
29. Lu N, Wang X, Suo Z, Vlassak J. Metal films on polymer substrates stretched beyond 50%. Applied Physics Letters. 2007;91(22).
30. Lu N, Wang X, Suo Z, Vlassak J. Failure by simultaneous grain growth, strain localization, and interface debonding in metal films on polymer substrates. Journal of Materials Research. 2009;24(2):379-85.
31. Niu RM, Liu G, Wang C, Zhang G, Ding XD, Sun J. Thickness dependent critical strain in submicron Cu films adherent to polymer substrate. Applied Physics Letters. 2007;90(16).
32. Xiang Y, Li T, Suo Z, Vlassak JJ. High ductility of a metal film adherent on a polymer substrate. Applied Physics Letters. 2005;87(16).
33. Yu DY, Spaepen F. The yield strength of thin copper films on Kapton. Journal of Applied Physics. 2004;95(6):2991-7.
34. Kraft O, Hommel M, Arzt E. X-ray diffraction as a tool to study the mechanical behaviour of thin films. Materials Science and Engineering. 2000;288(2):209-16.
35. Kreiml P, Rausch M, Terziyska VL, Köstenbauer H, Winkler J, Mitterer C, et al. Improved electro-mechanical reliability of flexible systems with alloyed Mo-Ta adhesion layers. Thin Solid Films. 2021;720:138533.
36. Jörg T, Cordill MJ, Franz R, Glushko O, Winkler J, Mitterer C. The electro-mechanical behavior of sputter-deposited Mo thin films on flexible substrates. Thin Solid Films. 2016;606:45-50.
37. Cordill MJ, Glushko O, Kreith J, Marx VM, Kirchlechner C. Measuring electro-mechanical properties of thin films on polymer substrates. Microelectronic engineering. 2015;137:96-100.
38. Li T, Huang Z, Suo Z, Lacour SP, Wagner S. Stretchability of thin metal films on elastomer substrates. Applied physics letters. 2004;85(16):3435-7.
39. Li T, Huang ZY, Xi ZC, Lacour SP, Wagner S, Suo Z. Delocalizing strain in a thin metal film on a polymer substrate. Mechanics of Materials. 2005;37(2-3):261-73.
40. Li T, Suo Z. Ductility of thin metal films on polymer substrates modulated by interfacial adhesion. International Journal of Solids and Structures. 2007;44(6):1696-705.

41. Blaber J, Adair B, Antoniou A. Ncorr: open-source 2D digital image correlation matlab software. Experimental Mechanics. 2015;55(6):1105-22.
42. Buch A. Pure metals properties: a scientific and technical handbook1999.
43. Abdel-Wahab AA, Ataya S, Silberschmidt VV. Temperature-dependent mechanical behaviour of PMMA: Experimental analysis and modelling. Polymer Testing. 2017;58:86-95.
44. Huo Y, Lee CC. The growth and stress vs. strain characterization of the silver solid solution phase with indium. Journal of Alloys and Compounds. 2016;661:372-9.
45. Savruk MP, Kazberuk A. A plane periodic boundary-value problem of elasticity theory for a half-plane with curvilinear edge. Materials Science. 2008;44(4):461-70.
46. Dorris JF, Nemat-Nasser S. Instability of a layer on a half space. 1980:304-12.
47. Hutchinson JW, Suo Z. Mixed mode cracking in layered materials. Advances in applied mechanics. 1991;29:63-191.
48. Steif PS. Bimaterial interface instabilities in plastic solids. International journal of solids and structures,. 1986;22(2):195-207.
49. Storen S, Rice JR. Localized necking in thin sheets. J Mech Phys Solids. 1975;23:421–41.